Journal of the European Ceramic Society 39 (2019) 30–40

Contents lists available at ScienceDirect

Journal of the European Ceramic Society

journal homepage: www.elsevier.com/locate/jeurceramsoc

Original Article

Oxygen transport, thermal and electrochemical properties of $NdBa_{0.5}Sr_{0.5}Co_2O_{5+\delta}$ cathode for SOFCs

Adi Subardi[a,b], Kun-Yu Liao[a], Yen-Pei Fu[a,*]

[a] Department of Materials Science & Engineering, National Dong Hwa University, Shou-Feng, Hualien, 97401, Taiwan
[b] Department of Mechanical Engineering, STTNAS, Yogyakarta, 55281, Indonesia

ARTICLE INFO

Keywords:
Solid oxide fuel cells
Oxygen migration mechanism
Oxygen permeation flux
Thermal properties
Long-term testing

ABSTRACT

In this study, the crystal structure, thermal, oxygen transport, electrical conductivity and electrochemical properties of the perovskite $NdBa_{0.5}Sr_{0.5}Co_2O_{5+\delta}$ (NBSC55) are investigated. In the temperature range of 250 °C–350 °C, the weight loss upon heating was due to a partial loss of lattice oxygen and along with a reduction of Co^{4+} to Co^{3+}. The tend of weight-loss slows down as temperature increased above 350 °C indicating a reduction of Co^{3+} to Co^{2+} during this stage. The oxygen migration is dominated by surface exchange process at high temperature range (650-800 °C); however, the bulk diffusion process prevails at low temperature range (500–600 °C). For long-term testing, the polarization resistance of NBSC55 increases gradually form 3.13 Ω cm^2 for 2 h to 3.34 Ω cm^2 for 96 h at 600 °C and an increasing-rate for polarization resistance is around 0.22% h^{-1}. The power density of the single cell with NBSC55 cathode reached 341 mW cm^{-2} at 800 °C.

1. Introduction

Recent studies paid attention to lower the operating temperature of solid oxide fuel cells (SOFCs) below 800 °C to improve long-term stability and reduce costs. However, lowering the operating temperature leads to a reduction in cell performance, largely due to the high activation energy of the oxygen reduction reaction of cathode [1,2]. There are two major strategies being adopted to enhance the cell power density at intermediate temperatures. One strategy is to minimize the ohmic loss by reducing the thickness of the electrolyte layer to 10 μm or below by developing anode-supported electrolyte cells [3]. The other is to reduce the electrode polarization loss by developing a high performance cathode [4]. Therefore, the exploitation of new electrodes with higher electrocatalytic activities is critical for IT-SOFCs [5,6]. Perovskite-type (ABO_3) ceramics with mixed ionic and electronic conductors (MIECs) have been widely investigated as potential cathodes for intermediate-temperature SOFCs (IT-SOFCs). There are some reports concerning the impressive oxygen reduction reaction (ORR) for oxygen-deficient layered perovskites, which show excellent electrocatalytic activity for the ORR at intermediate temperatures range [7–9]. Based on previous literature, oxygen surface sorption and bulk diffusion limit the characteristic depth of oxygen reduction in porous MIEC electrodes [10]. To improve the efficiency of SOFCs performance at reduced temperatures, cathode with faster oxygen diffusion rates through the material bulk and better surface exchange kinetics are vital. Substituted perovskite oxides have been the most thoroughly investigated oxides for these purposes [11].

In recent years, layered perovskites, $LnBaCo_2O_{5+\delta}$, have been extensively studied due to the facts that oxygen can easily and fast migrate through the LnO plane, and it was noticed via neutron diffraction technique and molecular dynamics simulations [12–14]. There are lots of studies doping lanthanides and/or alkali-earth metals into the A-site of the $LnBaCo_2O_{5+\delta}$ such as $SmBa_{0.5}Sr_{0.5}Co_2O_{5+\delta}$ [15–18], $YBa_{0.6}Sr_{0.4}Co_2O_{5+\delta}$ [19], $GdBa_{0.5}Sr_{0.5}Co_{2-x}Fe_xO_{5+\delta}$ [20,21], $PrBa_{0.5}Sr_{0.5}Co_{2-x}Fe_xO_{5+\delta}$ [22], $NdBa_{1-x}Sr_xCo_2O_{5+\delta}$ [23] to enhance the oxygen transport in the LnO plane. Kim et al. proposed that substitution of Sr for Ba in $GdBaCo_2O_{5+\delta}$ improved chemical stability between the cathode and electrolyte, and expedited oxygen transport [24]. Mckinlay et al. reported that the substitution of Sr for Ba resulted in a significant increase of conductivity in $YBaCo_2O_{5+\delta}$. The conductivity value of $YBa_{0.5}Sr_{0.5}Co_2O_{5+\delta}$ is much higher than $YBaCo_2O_{5+\delta}$, presumably due to the smaller lattice volume for Sr-substituted specimen [25]. Meng et al. reported that Sr doping in $YBaCo_2O_{5+\delta}$ enhance the electrical conductivity possibly due to the greater amount of electronic holes and mobile interstitial oxygen [26]. On the basis of these reports, it concludes that the $LnBaCo_2O_{5+\delta}$ substitution of Sr^{2+} for one-half of Ba^{2+} sites may result in higher electrical conductivity as well as better electrochemical performance.

In this study, we studied the effect of Nd and Sr substitution on layered perovskites $LnBaCo_2O_{5+\delta}$ with the formula,

* Corresponding author.
E-mail address: ypfu@gms.ndhu.edu.tw (Y.-P. Fu).

https://doi.org/10.1016/j.jeurceramsoc.2018.01.022
Received 1 September 2017; Received in revised form 15 December 2017; Accepted 15 January 2018
Available online 02 February 2018

$NdBa_{0.5}Sr_{0.5}Co_2O_{5+\delta}$ (NBSC55). The crystal structure, thermogravimetric property, oxygen non-stoichiometry, electrical conductivity, and electrochemical properties with long-term testing have been investigated. Moreover, to evaluate the oxygen-transportation properties, the oxygen permeation, oxygen migration mechanism, ionic conductivity, single cell performance were studied.

2. Experimental

2.1. Cathode and electrolyte materials preparation

The $NdBa_{0.5}Sr_{0.5}Co_2O_{5+\delta}$ (NBSC55) cathode powder was prepared via the solid-state reaction, where Nd_2O_3, $SrCO_3$, $BaCO_3$ and CoO powders were used as starting materials. The ball-milled mixture was dried and ground into a powder with mortar and pestle, and then calcined in air at 1100 °C for 4 h [27]. The $Ce_{0.8}Sm_{0.2}O_{1.9}$ (SDC) electrolyte powder was synthesized by co-precipitation using $Ce(NO_3)_3{\cdot}6H_2O$ and $Sm(NO_3)_3{\cdot}6H_2O$ as the starting materials. These starting materials with stoichiometric ratio were dissolved in distilled water and then added to a solution of ammonia. The pH value of the solution was adjusted to 9.5 ~ 10. Then, the coprecipitation powder was calcined in air to 600 °C for 2 h. The detailed procedure regarding the preparation of SDC can refer to reference [28].

2.2. Material characterization

The structure the sintered NBSC55 cathode was characterized by X-ray powder diffractometer (XRD; Rigaku D/MAX-2500V), with a scanning rate of 4°/min and scanning range of 20–80°, using a Cu K_α (1.5418 Å) radiation source. The powder pattern and lattice parameter were analyzed by Rietveld refinement. To understand the particle size distribution of NBSC55 powder, it was carried out using particle size analyzer (LS-POP (6), Beatop Electric Limited). This instrument works on the basis of light source of He-Ne laser with 2.0 mW. The instrument is capable to measure particle sizes distributed within a range of 0.2–500 μm. In this study, the distilled water was used as a solvent, and polyacrylic acid (PAA) was used as the dispersant. Thermogravimetric properties of NBSC55 cathode powder was performed by a thermogravimetric analyzer (TGA, SII TG/DTA 6300) in air with flow rate of 100 mL min^{-1}. The oxygen non-stoichiometry (δ) in air as a function of temperature was calculated based on the following equation [29].

$$\Delta\delta = \frac{M_s \Delta m}{M_o m} \quad (1)$$

where Δδ is the change in oxygen content, M_s is are the molar mass of the sample, M_o is the molar mass of oxygen, m is the sample mass at room temperature, Δm is the sample mass change after being heated, and the room temperature oxygen non-stoichiometry was determined by iodometric titration [30]. In order to investigate the oxygen vacancy concentration variation, the weight loss of the calcined powder were also performed from room temperature to 800 °C in N_2 with a constant heating rate of 10 °C/min. The thermal expansion coefficient (TEC) of the NBSC55 sintered at 1100 °C for 4 h was measured using a thermo-mechanical analyzer (TMA; Hitachi TMA7300) with a constant heating rate of 10 °C/min in the temperature range of 25–800 °C in a static air.

2.3. Oxygen permeation flux measurement

Oxygen permeation properties of NBSC55 membrane was measured using an in-house oxygen permeation. The membrane preparation is described below. The ball-milled calcined NBSC55 powder was press-formed into a disk diameter 13 mm and sintered at 1000 for 4 h in air. The membrane for oxygen permeation test was polished in the range of 0.8–1.4 mm in thickness, and sealed with gold ring between two quartz rods. The feed side fed with synthetic air (21 vol% O_2 + 79 vol% N_2) at a flow rate of 50 ml min^{-1}, while high pure He was applied to sweep side at a flow rate of 25 ml min^{-1}. An online-coupled Agilent 7890 gas chromatograph with a RT-Msieve 5A column was used to analyze the concentration of nitrogen and oxygen. The oxygen permeation flux was determined by the following equation [31].

$$J(O_2) = \left(C_{O_2} - \frac{0.21}{0.79}\sqrt{\frac{28}{32}}C_{N_2}\right)\frac{F}{S} \quad (2)$$

where $J(O_2)$ is the oxygen permeation flux (mL min^{-1} cm^{-2}), where C_{O_2} and C_{N_2} are the measured gas-phase concentrations in percentage of oxygen and nitrogen in the penetrative stream, respectively, F is the flow rate (mL min^{-1}) of the sweeping gas, and S is the effective surface area (cm^2) of the disk exposed to the sweeping gas. The measurement was conducted over a temperature range of 500–800 °C.

2.4. Symmetrical cell fabrication and measurement

A symmetrical cell of NBSC55 |SDC| NBSC55 configuration was fabricated by screen-printing technique. The NBSC55 cathode was pasted on both sides of SDC electrolyte discs in circles of 13 mm diameter and 1 mm thick. After the NBSC55 cathode was painted on the SDC electrolyte, it was sintered at 1000 °C for 4 h in air. The NBSC55 cathode was used as the working electrode (WE) with surface area of 0.385 cm^2. The Ag reference electrode (RE) was placed away from the WE by about 0.3–0.4 cm. The NBSC55 cathode counter electrode (CE) was placed on the other side of the SDC disk.

The symmetrical testing cell experiments were carried out under various oxygen partial pressures in temperatures ranged from 600 to 800 °C at intervals of 50 °C in air. The AC impedance measurement was performed using the VoltaLab PGZ301 potentiostat with frequency applied range from 100 kHz to 0.1 Hz with 10 mV AC signal amplitude. Under the cathodic polarized condition, the electrochemical impedance spectrometry (EIS) was conducted as a function of the applied cathodic voltage. For long-term testing, EIS was measured at 600 °C during 96 h in air. The EIS fitting analysis was performed with the Z-view software.

A NBSC55|SDC|Ni-SDC single cell performance was measured with humidified hydrogen (3 vol% H_2O) as the fuel and air as the oxidant to evaluate the performance of the fabricated anode-supported SOFCs. Anode substrates consisting of 58 wt% NiO, 38 wt% SDC and 4 wt% graphite were prepared by a die pressing process. SDC nanopowders were added onto the prepressed green NiO-SDC substrate. And then, the SDC powders and NiO-SDC substrate were co-pressed to form a green bilayer and subsequently co-sintered at 1400 °C for 4 h. Before the cathode was screen printed on electrolyte, the anode/electrolyte bilayer substrate have to anneal at 800 °C for 2 h in reducing atmosphere to reduce NiO to metallic Ni. Finally, NBSC55 was screen printed onto the SDC surface, and the resultant cell was sintered at 1000 °C for 4 h to form the porous cathode. The dimensions of a single cell is listed as follows: diameter of 13 mm, Ni-SDC anode thickness of 1 mm, SDC electrolyte thickness of 30 μm, and SBSC55 cathode thickness of 15–20 μm. Silver metal grids were applied as current collectors. The current-voltage characteristics of the single cell were collected using a digital source meter (Keithley 2420) at intervals of 100 °C over a temperature range of 600–800 °C.

3. Result and discussion

3.1. Crystal structure

The XRD pattern of NBSC55 after being calcined at 1100 °C for 4 h revealed in Fig. 1(a). Obviously, the pattern exhibited the double-perovskite structure without any peaks owing to impurities. The Rietveld refinement of NBSC55 including the measured, the calculated profile, and the difference between them depicted in Fig. 1(b). The experimental data and the calculated profiles are wonderful agreement, and the cations are well ordered between Nd^{3+} and Ba^{2+}/Sr^{2+} ions in the

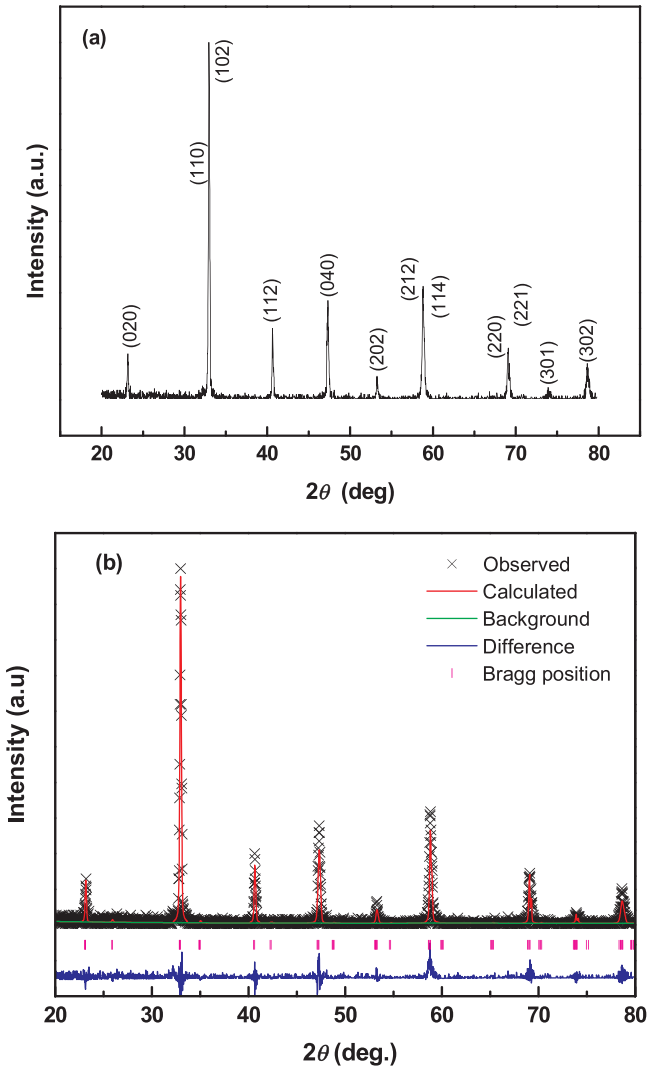

Fig. 1. (a) Room-temperature X-ray powder diffraction pattern; (b) Rietveld refinement of NBSC55 after being calcined at 1100 °C for 4 h. Observed (cross symbols), calculated (solid line) XRD profiles and the difference (bottom line) between them.

Table 1
Crystallographic information for NBSC55 calculated by Rietveld refinement.*

Atom	Wyckoff position	x	y	z	Uiso	Fractional occupancy
Nd1	1b (0 0 ½)	0	0	0.5	0.0100	0.9800
Ba2	1a (0 0 0)	0	0	0	0.0010	0.4920
Sr3	1a (0 0 0)	0	0	0	0.0102	0.5000
Co4	2h (½ ½ z)	0.5	0.5	0.2478	0.0092	1.0000
O5	1c (½ ½ 0)	0.5	0.5	0	0.0250	1.0000
O6	4i (½ 0 z)	0.5	0	0.2486	0.0250	1.0000
O7	1d (½ ½ ½)	0.5	0.5	0.5	0.0097	1.0000

* $R_p = 0.27$, $R_{wp} = 0.36$, $R_{exp} = 0.14$, Space group P 4/m m m (No. 123) - tetragonal, a = 3.861 Å, b = 3.861 Å, c = 7.715 Å, v = 115.01 Å^3.

ordered perovskite lattice [32]. Based on the diffraction pattern, NBSC55 is indexed to a tetragonal structure with space group: *P4/mmm*, lattice parameter: a = 3.86 Å, b = 3.86 Å, c = 7.72 Å and v = 115.01 Å^3. In NBSC55 structure, Nd atoms are resided at 1b (0, 0, 0.5) sites, Ba and Sr are distributed randomly over 1a (0, 0, 0) sites. While Co atoms are placed at 2 h (0.5, 0.5, 0.25) sites and O atoms are randomly distributed over 4i (0, 0.5, 0.25), 1c (0.5, 0.5, 0), and 1d (0.5, 0.5, 0.5) sites. Table 1 detailed the crystallographic information for NBSC55. Fig. 2 shows the particle size distribution of NBSC55 powder prepared by solid-state reaction technique calcined at 1100 °C, indicating the average particle size is about 2.6 μm as shown in SEM image.

3.2. Oxygen vacancy concentration variation and thermal expansion behavior

To determine the oxygen vacancy concentration variation of calcined NBSC55, the weight loss of specimen in air and N_2 atmosphere as a function of temperature is shown in Fig. 3(a). The oxygen vacancy concentration variation (ΔC_v) of the calcined powder at different temperature could be defined as follows [33].

$$\Delta C_v \approx \left(\frac{\rho}{M}\right)(\Delta W_{N_2}\% - \Delta W_{air}\%) \quad (3)$$

in which, ρ and *M* are the theoretical density (g/cm^3) and molar weight (g/mol) of the oxygen atom for the specimen, respectively; $\Delta W_{air}\%$, *and* $\Delta W_{N_2}\%$ are the percentage of weight difference in air and N_2 atmosphere, respectively. Based on Eq. (3), the oxygen vacancy concentration variation of the powder in air and N_2 atmosphere is shown in Fig. 3(b). A conspicuous weight gain is observed in the range of 220–280 °C in air. It is closely related to O_2 incorporation into oxygen vacancies resulting in the formation of lattice oxygen (O_o^x) accompanied by partial oxidation of cobalt ions from Co^{3+} to Co^{4+} as form of $Co_{Co}^{\cdot}$. As the temperature further increases above 300 °C, the Co—O bonds gradually broke and oxygen was released such as gained and original lattice oxygen. In this study, oxygen vacancy concentration variation is not obvious under 220 °C. However, the weight-loss in N_2 and weight-gain in air during the temperature range of 220–280 °C result in a significant oxygen vacancy concentration variation. The increase in oxygen vacancy concentration variations above 300 °C is due to the reduction of Co^{4+} ($Co^{4+} \rightarrow Co^{3+}$) with formation of plentiful amount of oxygen vacancy in air.

The thermal expansion coefficient (TEC) is a crucial property for cathodes as it impacts on the performance of a single cell. A bulk thermal expansion curve for NBSC55 cathode was carried out from room temperature to 800 °C using a thermomechanical analyzer and first derivative δL/L vs. temperature as shown in Fig. 3(c). The NBSC55 specimen seemingly shows a linear expansion in the temperature region of 100–800 °C. Actually, the thermal expansion curve could be divided into two regions, one is the low temperature region (100–250 °C); the other is the high temperature region (250–850 °C). The TEC value calculated from 100–800 °C for NBSC55 was $25.2 \times 10^{-6}\,K^{-1}$. The specimens show a linear expansion in the low temperature region (100–250 °C) with TEC value of $17.2 \times 10^{-6}\,K^{-1}$ and an increase in slope in the higher temperatures region (250–800 °C) with TEC value of $27.4 \times 10^{-6}\,K^{-1}$. The information about thermal expansion coefficient values of NBSC55 are detailed in Table 2. Generally, cobalt-based perovskite with a larger TEC values can be due to the increase of the ionic radius of Co during the thermal expansion measurement. As seen in the curve of $\frac{d\left(\frac{\delta L}{L}\right)}{dT}$ vs. temperature, there is an inflection region ranged from 230 to 300 °C. The inflection point may be associated to the initial temperature for the loss of lattice oxygen and the formation of oxygen vacancies [34]. At the same time, the reduction of the Co ion has to take place to maintain the electrical neutrality [35]. As the temperature is elevated above 250°C, a part of the Co^{4+} ions are reduced to Co^{3+} with a loss of oxygen; and Co^{3+} ions transit from low-spin ($t_{2g}^6 e_g^{\circ}$) to high-spin ($t_{2g}^4 e_g^2$) states [36,37]. The relationship based on the defect reaction using the Kroger-Vink notation is described as follows.

$$2Co_{Co}^{\cdot} + O_O^{\times} \leftrightarrow 2Co_{Co}^{\times} + V_O^{\cdot\cdot} + \frac{1}{2}O_2(\text{Co4} + \rightarrow \text{Co3} +) \quad (4)$$

The ionic radium of Co^{4+} and Co^{3+} with the coordination number of 6 and high spin are 0.53 and 0.61 nm, respectively [38]. The reduction of Co ions results in a decrease in the B—O bond according to Pauling's

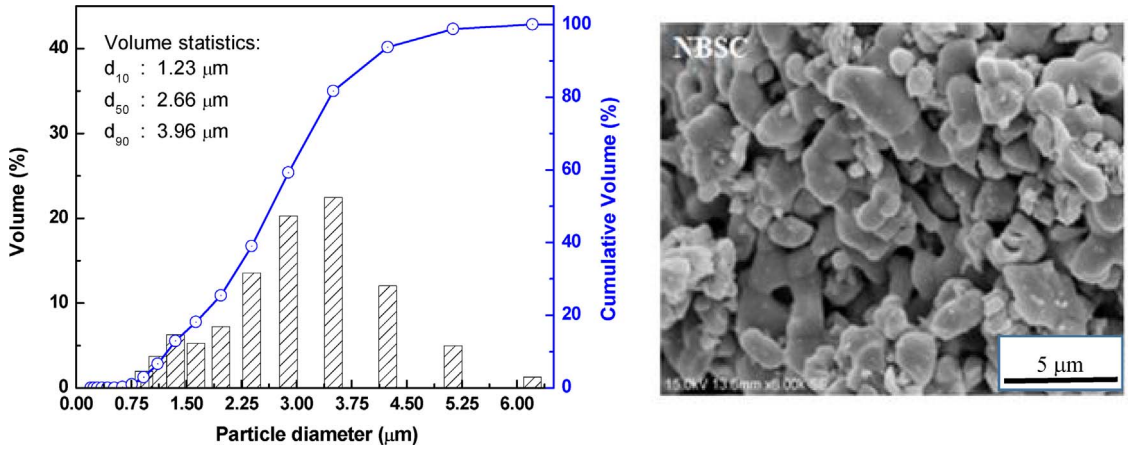

Fig. 2. Particle size distribution of NBSC55 powder prepared by solid-state reaction technique and its SEM image.

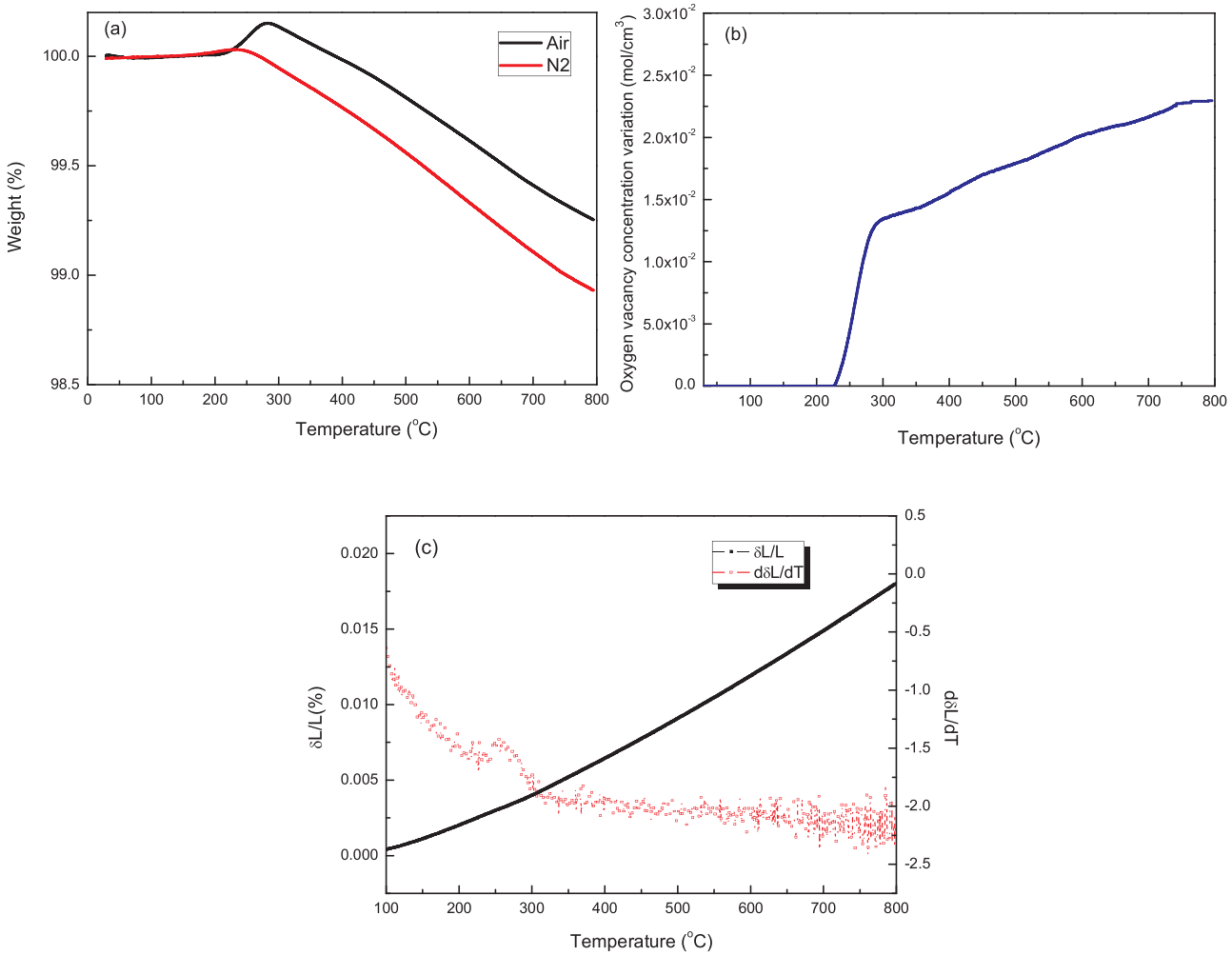

Fig. 3. Thermal properties: (a) Thermogravimetric results in air and N_2 with a constant heating rate of 10 °C/min; (b) oxygen vacancy concentration differences for calcined NBSC55 powder; (c) thermal expansion curve and first derivative δL/L vs. temperature for sintered NBSC55 specimen.

Table 2
TEC values of NBSC55 cathode.

Specimen	TEC (10^{-6} K^{-1})		
	100–800 °C	100–250 °C	250–800 °C
NBSC55	25.2	17.2	27.4

second rule, causing an increase in the size of BO_6 octahedra, therefore, the lattice expansion is enhanced [39,40].

3.3. Oxygen permeation flux and oxygen migration mechanism

The temperature dependence of the oxygen permeation flux (Jo_2) for NBSC membrane with 1.0 mm thickness under an air/He with oxygen partial pressure gradient over the temperature range of

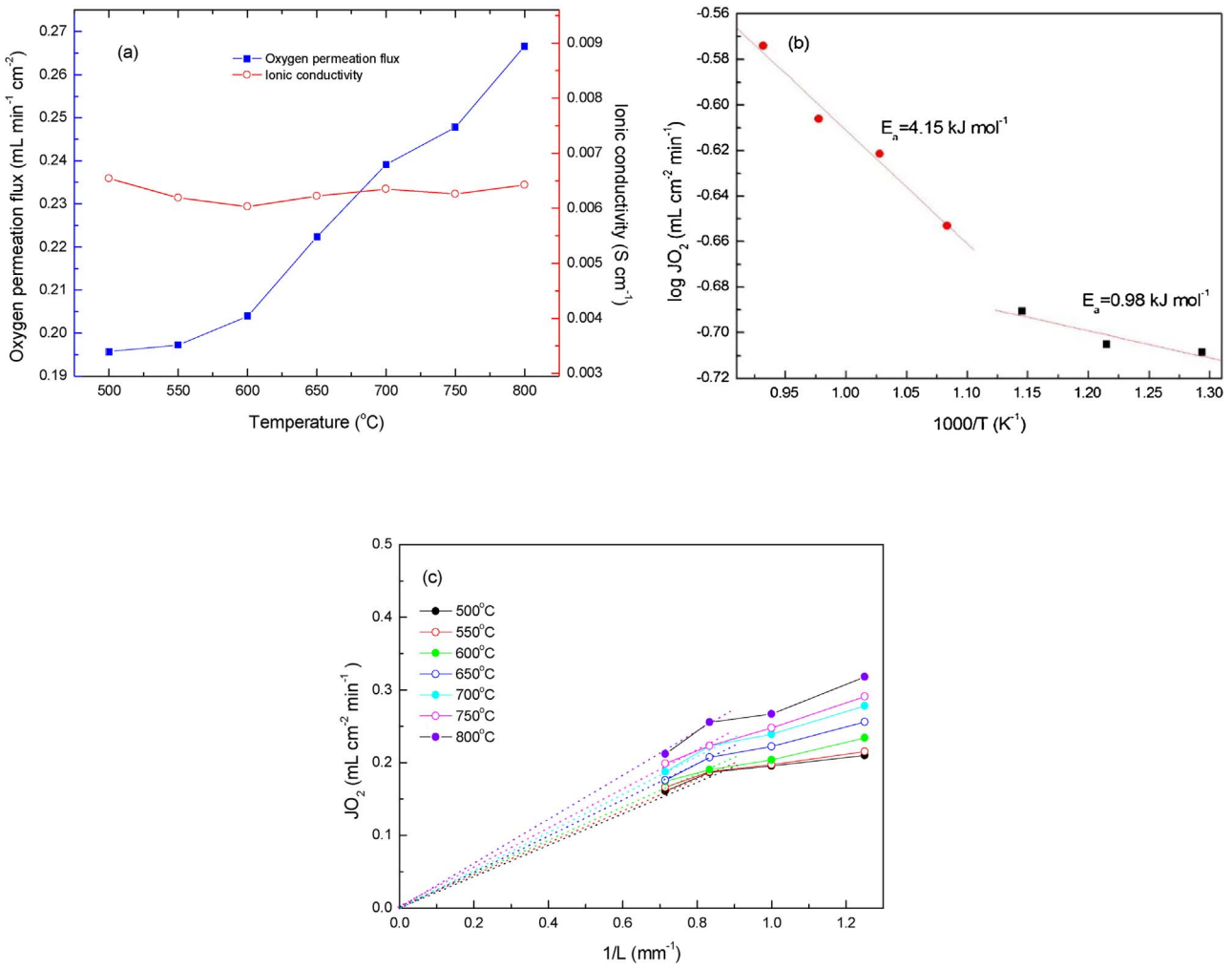

Fig. 4. (a) Oxygen permeation flux and nominal ionic conductivities as a function of temperature in thickness of 1.0 mm; (b) in the corresponding Arrhenius plot; (c) oxygen permeation flux as function of the reciprocal membrane thickness for NBSC55 membrane.

500–800 °C is shown in Fig. 4(a). The oxygen permeation flux raised from 0.198 mL min^{-1} cm^{-2} at 500 °C to 0.267 mL min^{-1} cm^{-2} at 800 °C under synthetic air with a flow rate of 50 mL min^{-1}, helium with a flow rate of 25 mL min^{-1}. The oxygen permeation flux increased steadily with temperature because of the increase in oxygen ionic bulk diffusion, the surface exchange rate and oxygen vacancy concentration [41,42]. The ionic conductivity could be estimated via using the Wagner relationship based on the following equation [43].

$$J(O_2) = \frac{RT}{16F^2L}\left(\frac{\sigma_e\sigma_i}{\sigma_e+\sigma_i}\right)(lnPo_2^{'}-lnPo_2^{''}) \quad (5)$$

where R is the ideal gas constant, L is the membrane thickness, T is the absolute temperature, F is the Faraday constant, σ_e is the electronic conductivity, σ_i is the oxygen ionic conductivity. $Po_2^{'}$ and $Po_2^{''}$ denote the oxygen partial pressure on the air side and the oxygen partial pressure on the sweep side, respectively. In this case, the electrical conductivity (σ_e) is significantly greater than ionic conductivity (σ_i).

The ionic conductivity can be calculated using the following equation.

$$\sigma_i = J(O_2)\frac{16F^2L}{RT}(ln\frac{P_{o2}^{'}}{P_{o2}^{''}})^{-1} \quad (6)$$

The ionic conductivities were distributed in the range of 6.03×10^{-3}–6.54×10^{-3} S cm^{-1}, it seems to be independent of as a function of temperature. The ionic conductivity of NBSC55 almost keep constant value. To further understand the oxygen migration process, the Arrhenius plot for oxygen permeation flux versus the reciprocal temperature was drawn as shown in Fig. 4(b). The Arrhenius plot could be divided into two temperature regions (500–600 °C and 650–800 °C). It implied that there are two different rate-determined processes (bulk diffusion process and slow surface exchange process) within two temperature regions. Generally, for the entire oxygen diffusion activation energy, the slow surface exchange process with a higher activation energy compared with the bulk diffusion process. Based on the calculation from the Arrhenius plot, the activation energies for the high-temperature region (650–800 °C) and low-temperature region (500–600 °C) are 4.15 and 0.98 kJ mol^{-1}, respectively. It suggested that surface exchange process with higher activation energy is dominated above 650 °C; whereas, when the temperature in the range of 500–600 °C, the bulk diffusion process with lower activation energy plays an important role.

In order to further understand the relationship in association with the oxygen migration mechanism and the membrane thickness, several membrane thicknesses (0.8 mm–1.4 mm) were prepared. Based on Eq. (5), the rate-limiting step of the oxygen permeation is the bulk diffusion. The relationship between oxygen permeation flux (Jo_2) and the reciprocal of the membrane thickness (1/L) should be a straight line passing through the origin of the coordinates [44]. When the membrane thickness is larger than 1.2 mm over the temperature range of 500–800 °C, oxygen permeation flux (Jo_2) is proportional to the reciprocal of the membrane thickness (1/L) as shown in Fig. 4(c). It

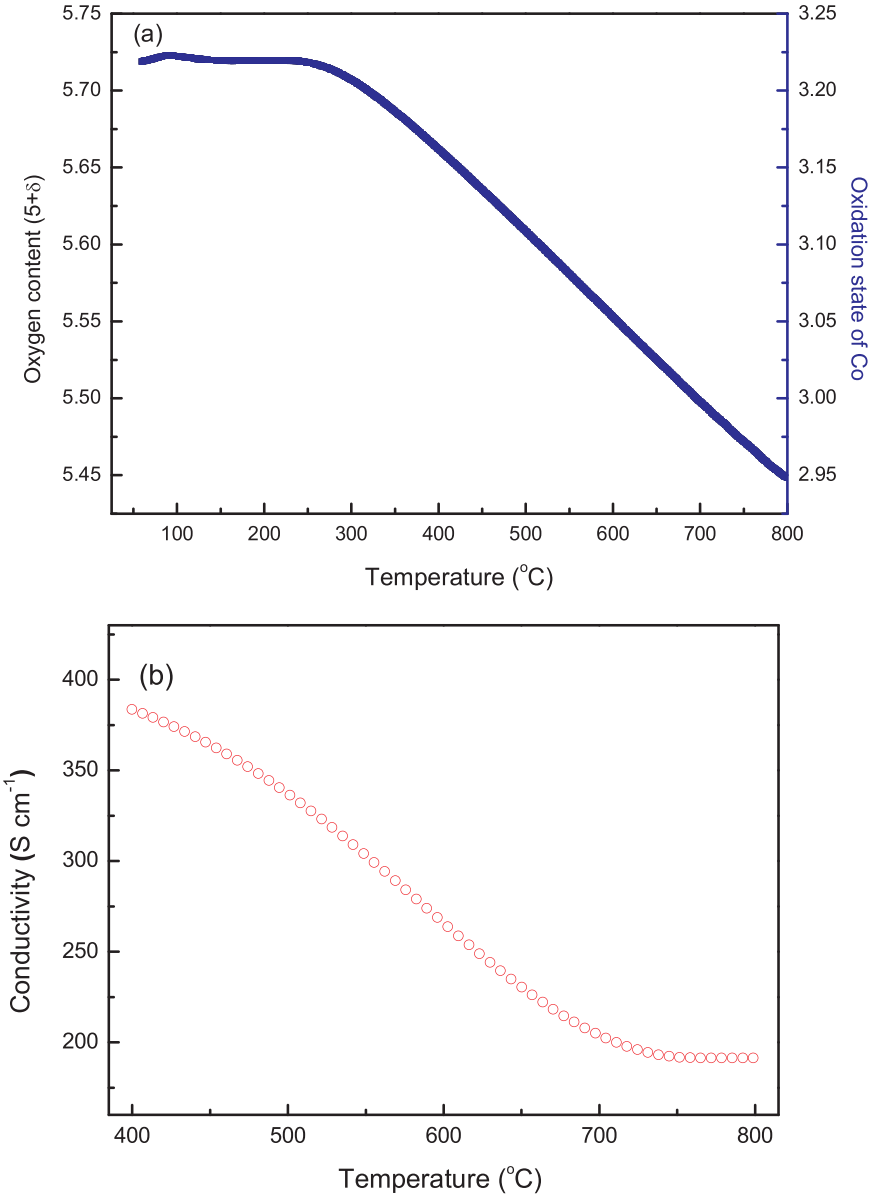

Fig. 5. (a) Oxygen content (5 + δ) and oxidation state of Co; (b) electrical conductivity as a function of temperature in air for NBSC55.

suggested that the oxygen permeation process is dominated by the bulk diffusion of oxygen ions as the membrane thickness is greater than 1.2 mm, On the contrary, as the membrane thickness is less than 1.2 mm, the oxygen permeation process is mostly governed by surface oxygen exchange.

3.4. Oxygen content (5 + δ) and electrical conductivity

Oxygen content (5 + δ) and oxidation state of Co for NBSC55 as a function of temperature in air is shown in Fig. 5(a). The slight weight loss from room temperature to 250 °C is due to desorption of the absorbed water from sample. As temperature ranged from 250 °C to 350 °C, the magnitude of weight reduced rapidly, implying that the specimen start to lose lattice oxygen significantly. The lattice oxygen was gradually removed and the additional oxygen vacancies were formed simultaneously [45]. The weight loss upon heating was due to a partial loss of lattice oxygen and along with a reduction of Co^{4+} to Co^{3+} from 250 °C to 350 °C. The weight-loss increase tend toward slows down as temperature increased from 350 °C to 1000 °C. It suggested that weight loss accompanied with a reduction of Co^{3+} to Co^{2+} during this stage [46–48]. Based on iodometric titration result, the initial oxygen content (5 + δ) is 5.72 at room temperature. The trend of oxygen content reveals as same as the weight loss as a function of temperature. It can be seen that the oxygen content, 5 + δ, decreased with temperature. The oxygen content of NBSC55 decreases gradually from 5 + δ = 5.72 at room temperature with Co valence-number of 3.22 to 5 + δ = 5.45 with Co valence-number of 2.95 at 800 °C. Table 3 detailed the oxygen-content (5 + δ) values and oxidation state of Co as a function of temperature in air.

Fig. 5(b) shows the electrical conductivity in air as a function of temperature for the dense NBSC55. The conductivity decreases with

Table 3
The oxygen content (5 + δ) and oxidation state of Co for NBSC55 as a function of temperature in air.

Specimen	NBSC55	
Temperature (°C)	Oxygen content (5 + δ)	Oxidation state of Co
200	5.72	3.22
400	5.66	3.16
600	5.55	3.05
800	5.45	2.95

increasing temperature exhibiting a metallic behavior. A gradual reduction of electrical conductivity from 384 S cm^{-1} of 400 °C to 202 S cm^{-1} of 700 °C due to lattice defects breaking the Co—O—Co bonds, resulting in escape of oxygen atoms from lattice and reduction of Co^{3+} to Co^{2+}, which corresponds to our previous TGA data. In this case, the major defects are the oxygen interstitials, O_i'' and the electronic holes, $h = Co_{Co}^{\bullet}$ [49]. Using the Kroger-Vink notation, the formation of the oxygen interstitials and electronic hole is expressed as below.

$$\frac{1}{2}O_2 + Co_{Co}^{\times}(\leftrightarrow)O_i^{''} + 2Co_{Co}^{\bullet} \quad (7)$$

The electrical neutrality condition is given by

$$2[O_i^{''}] = [Co_{Co}^{\bullet}] \quad (8)$$

The apparent metallic conductivity behavior of NBSC55 may be related to the following reasons [50–52]: (1) an energy band overlap between Co-3d and O-2p; (2) the presence of Co^{3+} ions from thermally generated charge disproportion of Co^{2+} along with the loss of oxygen from the lattice simultaneously at higher temperatures. As the temperature is greater than 750 °C, the electrical conductivity revealed stable value about 191 S cm^{-1}. This means that the electronic hole concentration no more decreased above 750 °C. Over the temperature range of 400–800 °C, the electrical conductivity is above 100 S cm^{-1} indicating that NBSC55 could meet the requirement of electrical conductivity as an IT-SOFC cathode.

3.5. Impedance spectra as function of oxygen partial pressures and long-term testing

In order to further investigate the process of oxygen reduction reaction for NBSC55 cathode, EIS was investigated at different oxygen partial pressures. In general, the interfacial polarization resistance (R_P) changes with P_{O_2} can be described by the following equation [53,54]:

$$Rp = R_P^0(P_{O_2})^{-n} \quad (9)$$

The overall oxygen reduction reaction could be expressed as follow.

$$\frac{1}{2}O_2(g) + 2e^{'} = O^{2-} \quad (10)$$

The processes are complex containing charge transfer, surface adsorption/dissociation, gas diffusion, and so on. The magnitude of n provides valuable information about the rate-limiting step in the oxygen reduction reactions at cathodes [55,56]:

$$n = 0.10,\ O_O^x \Leftrightarrow O2{-}TPB + 2TB + VO \quad (11)$$

$$n = 0.25,\ Oads. + 2e^{'} + V_O^{''} \Leftrightarrow O_O^x \quad (12)$$

$$n = 0.50,\ O_{2,\ ads.} \Leftrightarrow 2O_{ads.} \quad (13)$$

$$n = 1.00,\ O_2(g) \Leftrightarrow O_{2,\ ads.} \quad (14)$$

where n = 0.10 has been associated with oxygen ion transfer from triple–phase boundary (TPB) to the electrolyte, n = 0.25 with the charge transfer processes, n = 0.50 with oxygen adsorption/desorption processes, and n = 1.00 with gas phase diffusion of oxygen molecules in a porous cathode. However, the entire surface may sever as the active sites for ORR in MIEC conductors. It is due to the facts that oxygen ions transport through the MIEC bulk [57,58]. In Eq. (11), the oxygen ion transfer is not only form TPB sites but also two-phase boundary (2PB) sites (cathode/electrolyte interface). The R_P dependence of P_{O_2} for NBSC55 measured at various temperatures are shown in Fig. 6(a). Clearly, the R_P values raised with reducing $P(O_2)$. This behavior is because of the decrease in mobile interstitial oxygen at lower $p(O_2)$. Based on slopes of log(R_P) vs. log(P_{O2}), the n value decreased from 600 °C of n = 0.25 to 800 °C of n = 0.13. This indicated that the rate-limiting process of ORR dominated by charger transfer ($O_{ads.} + 2e^{'} + V_O^{''} \Leftrightarrow O_O^x$)

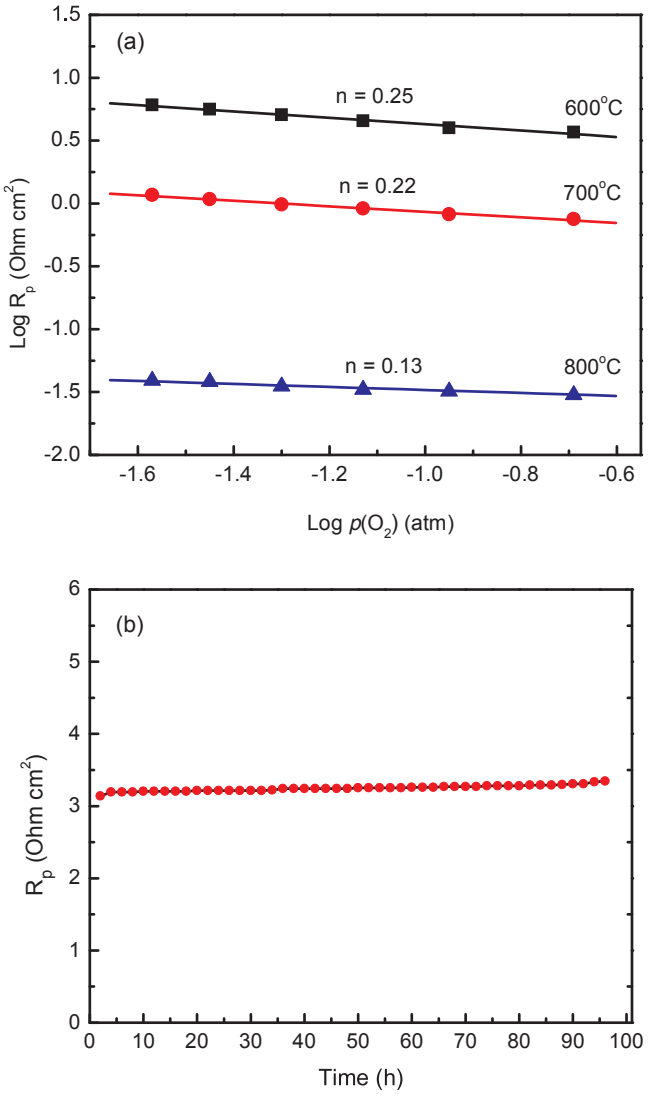

Fig. 6. (a)The interfacial polarization resistance (R_P) of NBSC55|SDC|NBSC55 half-cell dependence of oxygen partial pressure in the temperature range of 600–800 °C; (b) polarization resistance (R_p) of under static air at 600°C for long-term testing.

gradually transfers to oxygen ion transfer from TPB and/or 2PB sites of cathode ($O_O^x \Leftrightarrow O_{TPB}^{2-} + V_O^{\cdot\cdot}$) as the temperature increasing from 600 °C to 800 °C. It implied that overall ORR accomplished at 800°C in air.

To evaluate the stability the NBSC55 for a long time, the performance of a NBSC55 | SDC| NBSC55 half-cell was tested, and R_p values were recorded dependence of time under stationary air at 600 °C as shown in Fig. 6(b). Markedly, R_p increased gradually with time, which values were increased form 3.13 Ω cm^2 for the initial 2 h to 3.34 Ω cm^2 for 96 h long-term testing at 600 °C. A slight increase in cathodic polarization resistance is observed that an increasing-rate is around 0.22% h^{-1} from the initial 2 h to 96 h. Cathode delamination from electrolyte may be one possible cause of increasing in polarization resistance at initial fast degradation. Based on our group previous research, the difference in thermal expansion coefficient between NBSC55 (TEC = 25.2 ppm K^{-1}) and SDC (TEC = 12.4 ppm K^{-1}) is approximately 12.8 ppm K^{-1} [59]. The delamination between layers causes the decline of reaction sites for ORR, leading to increase polarization resistance. With increasing the testing time, the following slow degradation in the MIEC-cathode performance may be several possible mechanisms such as (1) the grain size of NBSC55 may coarsen [60], (2) interdiffusion may occur between NBSC55 and SDC interface [61], and (3) Sr may segregate from Sr-contained cathode [62].

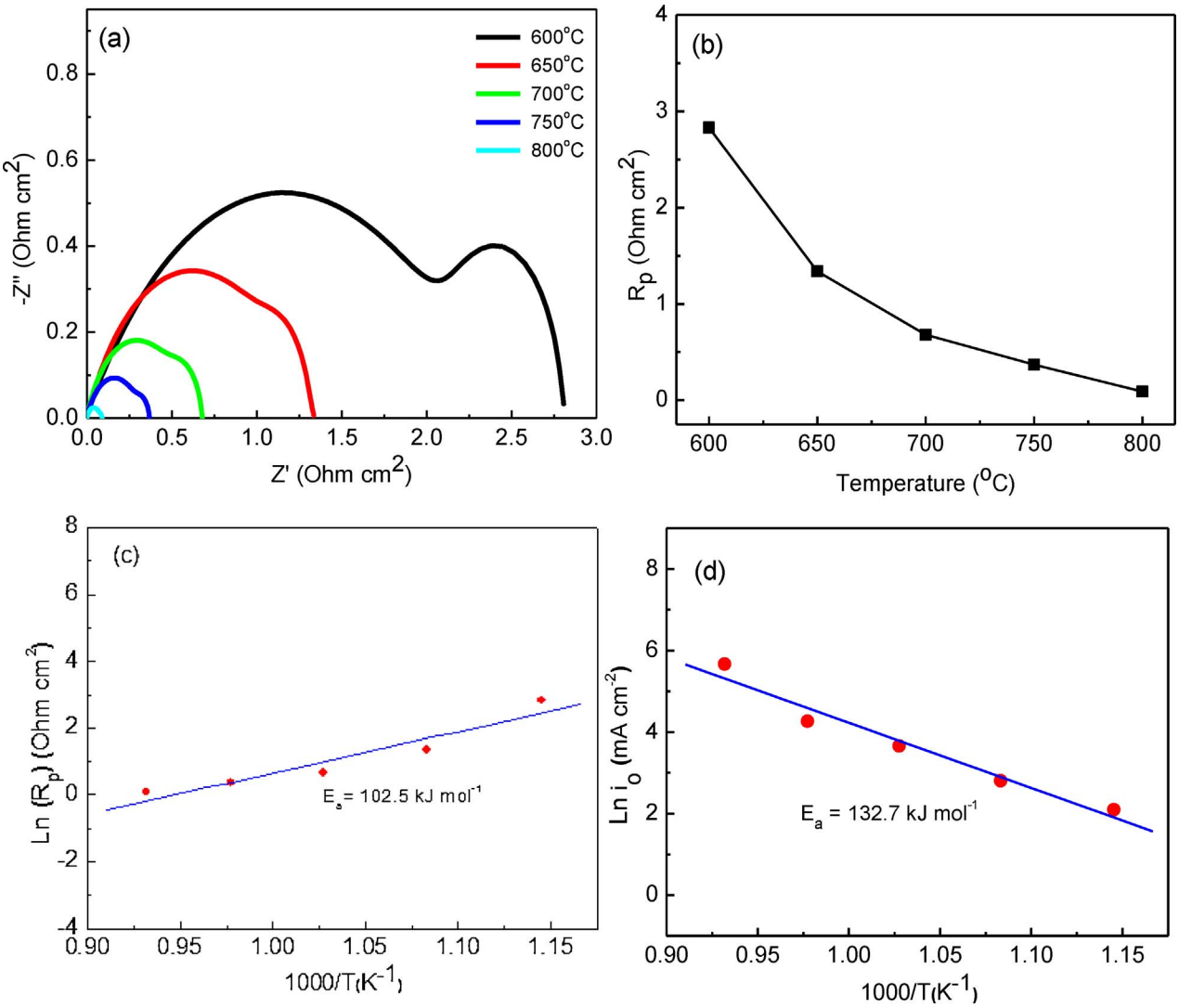

Fig. 7. (a) Nyquist plots of EIS; (b) interfacial resistance as a function of temperature; (c) Ln(R_p) vs. 1000/T; (d) Arrhenius plots of oxygen reduction reaction for NBSC55 cathode on SDC electrolyte over the temperature range of 600–800 °C.

3.6. Interfacial polarization resistance and a single cell performance

Cathode electrochemical properties were investigated by the AC impedance spectroscopy based on a NBSC55 |SDC| NBSC55 symmetrical cell. Interfacial polarization resistance of NBSC55 cathode was measured directly from the difference between high-and low-frequency intercepts on the real axis of the impedance plot [63]. Fig. 7(a) shows the impedance spectra measured under open-circuit conditions over the temperature range of 600–800 °C in air. In this study, the electrolyte/cathode interfacial polarization resistance was represented by area specific resistance (ASR). The cathode polarization resistance (R_p) was decreased markedly from 2.83 Ω cm^2 at 600°C to 0.09 Ω cm^2 at 800 °C for NBSC55 cathode as shown in Fig. 7(b). The activation energies (E_a) of cathode polarization resistance from Ln (R_p) vs. 1000/T plot was 102.5 kJ mol^{-1} as shown in Fig. 7(c). The detailed information regarding the technique could refer to our group published paper [27]. The i_o values were increased from 6.6 mA cm^{-2} of 600 °C to 256.8 mA cm^{-2} of 800 °C for EIS technique. The overall activation energy (E_a) for the ORR was identified from the slope of the Arrhenius plot as shown in Fig. 7(d). The E_a calculated from the plot for Ln (i_0) versus 1000/T was 132.7 kJ mol^{-1}. The E_a value is relatively similar to our previous report as cited in reference [27]. Fig. 8(a) displays the power density and voltage as a function of the current density for the NBSC55|SDC|Ni-SDC anode supported cell using hydrogen as a fuel and air as an oxidant in a temperature range of 600–800 °C. The power densities of the single cell were 45, 138 and 341 mW cm^{-2} at 600 °C, 700 °C, 800 °C, respectively. Based on literatures, the power density values of layered perovskite cathodes have been reported such as, $Nd_{0.96}BaCo_2O_{6-\delta}$, the powder density is 600 mW cm^{-2} at 700 °C [64], for $SmBa_{0.75}Ca_{0.25}CoFeO_{5+\delta}$ is 366 mW cm^{-2} at 800 °C [65]. In this study, the highest powder-density reached 341 mW cm^{-2} that is closed to 366 mW cm^{-2} of $SmBa_{0.75}Ca_{0.25}CoFeO_{5+\delta}$ at 800 °C. However, the powder density is lower than 760 mW cm^{-2} for $NdBa_{0.5}Sr_{0.5}Co_{1.5}Fe_{0.5}O_{5+\delta}$ at 650 °C [66], it may be ascribed to the following reasons: (1) the higher polarization resistance of NBSC55, (2) the delamination between SDC electrolyte and NBSC55 cathode due to higher TEC of cathode. Fig. 8 (b) exhibits SEM image of cross-sectional microstructure of NBSC55|SDC|Ni-SDC anode supported single cell after electrochemical measurement. The SDC electrolyte is highly dense with a thickness of 30 μm. The NBSC55 cathode reveals well-necked particles with an average size about 2–3 μm and moderate porosity that facilitating the gas diffusion from cathode to electrolyte. The thickness of the NBSC55 cathode layer was about 15 μm. Moreover, the Ni-SDC anode is porous, and the particles are well conjoined.

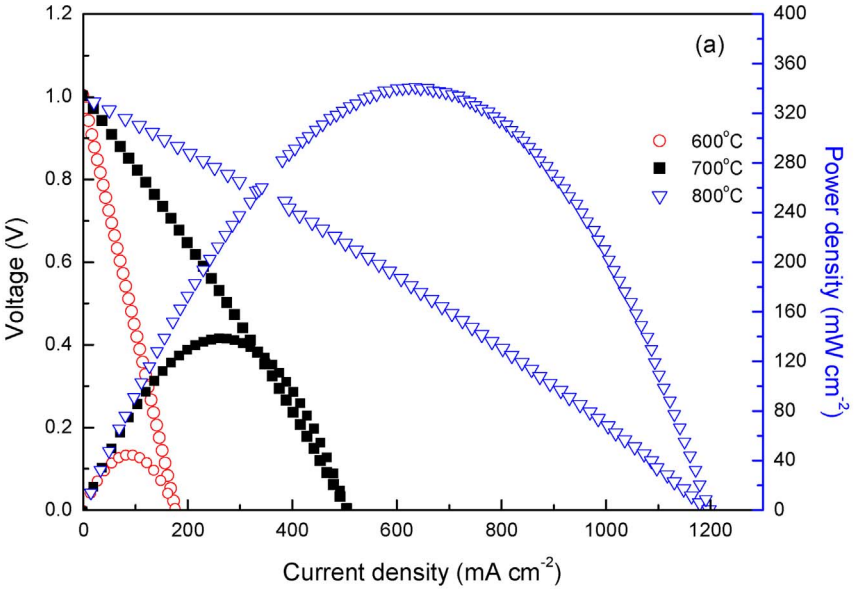

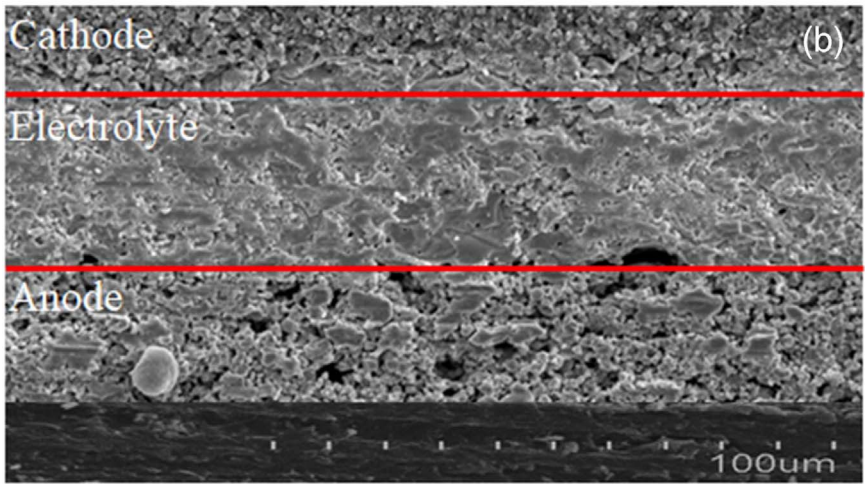

Fig. 8. (a) Cell performance and (b) SEM image for a NBSC55|SDC|Ni-SDC single cell.

4. Conclusions

The structural characteristics, thermogravimetric behavior, oxygen non-stoichiometry, oxygen permeation, oxygen migration mechanism, electrical conductivity and electrochemical properties for long-term testing of layered perovskite $NdBa_{0.5}Sr_{0.5}Co_2O_{5+\delta}$ have been studied in this work. The weight loss upon heating was due to a partial loss of lattice oxygen and along with a reduction of Co^{4+} to Co^{3+} from 250 °C to 350 °C. The weight-loss increase tend toward slows down as temperature increased from 350 °C to 1000 °C indicating that weight loss accompanied with a reduction of Co^{3+} to Co^{2+} during this stage. The electrical conductivity decreases with increasing temperature from 384 S cm^{-1} of 400 °C to 202 S cm^{-1} of 700 °C. This metallic-like behavior is ascribed to lattice defects breaking the Co—O—Co bonds, resulting in escape of oxygen atoms from lattice and reduction of Co^{3+} to Co^{2+}.

Based on the oxygen permeation flux versus temperature results, it could be conclude that the oxygen migration is dominated by surface exchange process at high temperature range, and the bulk diffusion process plays an important role at low temperature range. As for the effect of membrane thickness on oxygen process, it concluded that oxygen permeation process is dominated by the bulk diffusion of oxygen ions as the membrane thickness is greater than 1.2 mm, On the contrary, as the membrane thickness is less than 1.2 mm, the oxygen permeation process is mostly governed by surface oxygen exchange.

For long-term testing, polarization resistance was gradually increased form 3.13 Ω cm^2 for the initial 2 h to 3.34 Ω cm^2 for 96 h long-term testing at 600 °C with an increase rate of 0.22% h^{-1}. The impedance spectra as function of oxygen partial pressures revealed that n value decreased from 600 °C of n = 0.25 to 800 °C of n = 0.13. This implied that the rate-limiting process of ORR is dominated by charger transfer ($O_{ads.} + 2e' + V_O'' \Leftrightarrow O_O^x$) gradually transfers to oxygen ion transfer from TPB and/or 2PB sites of cathode ($O_O^x \Leftrightarrow O_{TPB}^{2-} + V_O^{\cdot\cdot}$) as the temperature increasing from 600 °C to 800 °C.

Acknowledgement

The authors are grateful for the financial support of this research by Ministry of Science and Technology of Taiwan under contract number: MOST 106-2113-M-259-011.

References

[1] L. Ding, L. Wang, D. Ding, S. Zhang, X. Ding, G. Yuan, Promotion on electrochemical performance of a cation deficient $SrCo_{0.7}Nb_{0.1}Fe_{0.2}O_{3-\delta}$ perovskite cathode for intermediate-temperature solid oxide fuel cells, J. Power Sources 354 (2017) 26–33.

[2] E.D. Wachsman, K.T. Lee, Lowering the temperature of solid oxide fuel cells, Science 334 (2011) 935–939.
[3] L.C. De Jonghe, C.P. Jacobson, S.J. Visco, Supported electrolyte thin film synthesis of solid oxide fuel cells, Ann. Rev. Mater. Res. 33 (2003) 169–182.
[4] K. Chen, N. Li, N. Ai, M. Li, Y. Cheng, W.D.A. Rickard, J. Li, S.P. Jiang, Direct application of cobaltite-based perovskite cathodes on the yttria-stabilized zirconia electrolyte for intermediate temperature solid oxide fuel cells, J. Mater. Chem. A 4 (2016) 17678–17685.
[5] A. Giuliano, M.P. Carpanese, M. Panizza, G. Cerisola, D. Clematis, A. Barbucci, Characterisation of $La_{0.6}Sr_{0.4}Co_{0.2}Fe_{0.8}O_{3-\delta}$ – $Ba_{0.5}Sr_{0.5}Co_{0.8}Fe_{0.2}O_{3-\delta}$ composite as cathode for solid oxide fuel cells, Electrochim. Acta 240 (2017) 258–266.
[6] A. Giuliano, C. Nicollet, S. Fourcade, F. Mauvy, M.P. Carpanese, J.-C. Grenier, Influence of the electrode/electrolyte interface structure on the performance of $Pr_{0.8}Sr_{0.2}Fe_{0.7}Ni_{0.3}O_{3-\delta}$ as solid oxide fuel cell cathode, Electrochim. Acta 236 (2017) 328–336.
[7] C.C. Duan, D. Hook, Y.C. Chen, J.H. Tong, R. O'Hayre, Zr and Y co-doped perovskite as a stable, high performance cathode for solid oxide fuel cells operating below 500 degrees C, Eng. Environ. Sci. 10 (2017) 176–182.
[8] Z. Yang, Y. Liu, Y. Chen, J. Wang, Z. Han, Y. Zhu, M. Han, Effects of humidity on $Ba_{0.9}Co_{0.7}Fe_{0.2}Nb_{0.1}O_{3-\delta}$ cathode performance and durability of solid oxide fuel cells, Int. J. Hydrogen Energy 42 (2017) 6997–7002.
[9] T.H. Lee, K.Y. Park, N.I. Kim, S.J. Song, K.H. Hong, D. Ahn, A.K. Azad, J. Hwang, S. Bhattacharjee, S.C. Lee, H.T. Lim, J.Y. Park, Robust $NdBa_{0.5}Sr_{0.5}Co_{1.5}Fe_{0.5}O_{5+\delta}$ cathode material and its degradation prevention operating logic for intermediate temperature-solid oxide fuel cells, J. Power Sources 331 (2016) 495–506.
[10] S.B. Adler, Factors governing oxygen reduction in solid oxide fuel cell cathode, Chem. Rev. 104 (2004) 4791–4843.
[11] X. Song, S. Le, X. Zhu, L. Qin, Y. Luo, Y. Li, K. Sun, Y. Chen, High performance $BaFe_{1-x}Bi_xO_{3-\delta}$ as cobalt-free cathodes for intermediate temperature solid oxide fuel cells, Int. J. Hydrogen Energy 42 (2017) 15808–15817.
[12] C. Frontera, A. Caneiro, A.E. Carrillo, J. Oró-Solé, J.L. García-Mu˜noz, Tailoring oxygen content on $PrBaCo_2O_{5+\delta}$ layered cobaltites, Chem. Mater. 17 (2005) 5439–5445.
[13] D. Parfitt, A. Chroneos, A. Tarancón, J.A. Kilner, Oxygen ion diffusion in cation ordered/disordered $GdBaCo_2O5+\delta$, J. Mater. Chem. 21 (2011) 2183–2186.
[14] A.C. Tomkiewicz, M.A. Tamimi, A. Huq, S. McIntosh, Structural analysis of $PrBaMn_2O_{5+\delta}$ under SOFC anode conditions by in-situ neutron powder diffraction, J. Power Sources 330 (2016) 240–245.
[15] A. Subardia, C.C. Chen, M.H. Cheng, W.K. Chang, Y.P. Fu, Electrical, thermal and electrochemical properties of $SmBa_{1-x}Sr_xCo_2O_{5+\delta}$ cathode materials for intermediate-temperature solid oxide fuel cells, Electrochim. Acta 204 (2016) 118–127.
[16] J.H. Kim, M. Cassidy, J.T.S. Irvine, J. Bae, Electrochemical investigation of composite cathodes with $SmBa_{0.5}Sr_{0.5}Co_2O_{5+\delta}$ cathodes for intermediate temperature-operating solid oxide fuel cell, Chem. Mater. 22 (2010) 883–892.
[17] A. Jun, J. Kim, J. Shin, G. Kim, Optimization of Sr content in layered $SmBa_{1-x}Sr_xCo_2O_{5+\delta}$ perovskite cathodes for intermediate-temperature solid oxide fuel cells, Int. J. Hydrogen Energy 37 (2012) 18381–18388.
[18] B. Wang, G. Long, Y. Li, Y. Ji, Characterization of $SmBa_{0.5}Sr_{0.5}CoCuO_{5+\delta}$ cathode based on GDC and LSGM electrolyte for intermediate-temperature solid oxide fuel cells, Int. J. Hydrogen Energy 41 (2016) 13603–13610.
[19] J. Xue, Y. Shen, T. He, Performance of double-proveskite $YBa_{0.5}Sr_{0.5}Co_2O_{5+\delta}$ as cathode material for intermediate-temperature solid oxide fuel cells, Int. J. Hydrogen Energy 36 (2011) 6894–6898.
[20] C. Kuroda, K. Zheng, K. Swierczek, Characterization of novel $GdBa_{0.5}Sr_{0.5}Co_{2-x}Fe_xO_{5+\delta}$ perovskites for application in IT-SOFC cells, Int. J. Hydrogen Energy 38 (2013) 1027–1038.
[21] J. Kim, A. Jun, J. Shin, G. Kim, Effect of Fe doping on layered $GdBa_{0.5}Sr_{0.5}Co_2O_{5+\delta}$ perovskite cathodes for intermediate temperature solid oxide fuel cells, J. Am. Ceram. Soc. 97 (2014) 651–656.
[22] L. Jiang, T. Wei, R. Zeng, W.X. Zhang, Y.H. Huang, Thermal and electrochemical properties of $PrBa_{0.5}Sr_{0.5}Co_{2-x}Fe_xO_{5+\delta}$ ($x = 0.5, 1.0, 1.5$) cathode materials for solid-oxide fuel cells, J. Power Sources 232 (2013) 279–285.
[23] J.H. Kim, J.T.S. Irvine, Characterization of layered perovskite oxides $NdBa_{1-x}Sr_xCo_2O_{5+\text{delta}}$ ($x = 0$ and 0.5) as cathode materials for IT-SOFC, Int. J. Hydrogen Energy 37 (2012) 5920–5929.
[24] J.H. Kim, F. Prado, A. Manthiram, Characterization of $GdBa_{1-x}Sr_xCo_2O_{5+\delta}$ ($0 \leqslant x \leqslant 1.0$) double perovskites as cathodes for solid oxide fuel cells, J. Electrochem. Soc. 155 (2008) B1023–B1028.
[25] A. McKinlay, P. Connor, J.T.S. Irvine, W.Z. Zhou, Structural chemistry and conductivity of a solid solution of $YBa_{1-x}Sr_xCo_2O5+\delta$, J. Phys. Chem. C 111 (111) (2007) 19120–19125.
[26] F. Meng, T. Xia, J. Wang, Z. Shi, J. Lian, H. Zhao, J.M. Bassat, J.C. Grenier, Evaluation of layered perovskites $YBa_{1-x}Sr_xCo_2O_{5+\delta}$ as cathodes for intermediate temperature solid oxide fuel cells, Int. J. Hydrogen Energy 39 (2014) 4531–4543.
[27] A. Subardi, M.H. Cheng, Y.P. Fu, Chemical bulk diffusion and electrochemical properties of $SmBa_{0.6}Sr_{0.4}Co_2O_{5+\delta}$ cathode for intermediate solid oxide fuel cells, Int. J. Hydrogen Energy 39 (2014) 20783–20790.
[28] Y.P. Fu, S.B. Wen, C.H. Lu, Preparation and characterization of samaria-doped ceria electrolyte materials for solid oxide fuel cells, J. Am. Ceram. Soc. 91 (2008) 127–131.
[29] M. Kuhn, J.J. Kim, S.R. Bishop, H.L. Tuller, Oxygen nonstoichiometry and defect chemistry of perovskite-structured $Ba_xSr_{1-x}Ti_{1-y}Fe_yO_{3-y/2+\delta}$ solid solutions, Chem. Mater. 25 (2013) 2970–2975.
[30] R.J. Nadalin, W.B. Brozda, Chemical methods for the determination of the"oxidizing (or reducing) power"of certain materials containing a multivalent element in several oxidation states, Anal. Chim. Acta 28 (1963) 282–293.
[31] Y. Chen, B. Qian, S. Li, Y. Jiao, M.O. Tade, Z. Shao, The influence of impurity ions on the permeation and oxygen reduction properties of $Ba_{0.5}Sr_{0.5}Co_{0.8}Fe_{0.2}O_{3-\delta}$ perovskite, J. Membr. Sci. 449 (2014) 86–96.
[32] A. Jun, J. Shin, G. Kim, High redox and performance stability of layered $SmBa_{0.5}Sr_{0.5}Co_{1.5}Cu_{0.5}O_{5+\delta}$ perovskite cathodes for intermediate-temperature solid oxide fuel cells, Phys. Chem. Chem. Phys. 15 (2013) 19906–19912.
[33] S. Lia, W. Jin, N. Xu, J. Shi, Mechanical strength, and oxygen and electronic transport properties of $SrCo_{0\text{-}4}Fe_{0\text{-}6}O_{3-\delta}$-YSZ membranes, J. Membr. Sci. 186 (2001) 195–204.
[34] Y. Teraoka, M. Yoshimatsu, N. Yamazoe, T. Seiyama, Oxygen-sorptive properties and defect structure of perovskite-type oxides, Chem. Lett. (1984) 893–896.
[35] A.L. Shaula, V.V. Kharton, N.P. Vyshatko, E.V. Tsipis, M.V. Patrakeev, F.M.B. Marques, J.R. Frade, Oxygen ionic transport in $SrFe_{1-y}Al_yO_{3-\delta}$ and $Sr_{1-x}Ca_xFe_{0.5}Al_{0.5}O_{3-\delta}$ ceramics, J. Eur. Ceram. Soc. 25 (2005) 489–499.
[36] K. Huang, H.Y. Lee, J.B. Goodenough, Sr- and Ni-doped $LaCoO_3$ and $LaFeO_3$ perovskites new cathode materials for solid-oxide fuel cells, J. Electrochem. Soc. 145 (1998) 3220–3227.
[37] M.A. Senaris-Rodriguez, J.B. Goodenough, $LaCoO_3$ revisited, J. Solid State Chem. 116 (1995) 224–231.
[38] R.D. Shannon, Revised effective ionic radii and systematic studies of interatomic distances in halides and chalcogenides, Acta Crystallogr. A 32 (1976) 751–767.
[39] G.Ch. Kostogloudis, P. Fertis, Ch. Ftikos, The perovskite oxide system $Pr_{1-x}Sr_xCo_{1-y}Mn_yO_{3-\delta}$: crystal structure and thermal expansion, J. Eur. Ceram. Soc. 18 (1998) 2209–2215.
[40] B. Wei, Z. Lu, X. Huang, J. Miao, X. Sha, X. Xin, W. Su, Crystal structure, thermal expansion and electrical conductivity of perovskite oxides $Ba_xSr_{1-x}Co0.Fe_{0.2}O_{3-\delta}$ ($0.3 \leq x \leq 0.7$), J. Eur. Ceram. Soc. 26 (2006) 2827–2832.
[41] D. Han, J. Wu, Z. Yan, K. Zhang, J. Liu, S. Liu, $La_{0.6}Sr_{0.4}Co_{0.2}Fe_{0.8}O_{3-\delta}$ hollow fibre membrane performance improvement by coating of $Ba_{0.5}Sr_{0.5}Co_{0.9}Nb_{0.1}O_{3-\delta}$ porous layer, RSC Adv. 4 (2014) 19999–20004.
[42] J. Yang, H. Zhao, X. Liu, Y. Shen, L. Xu, Bismuth doping effects on the structure, electrical conductivity and oxygen permeability of $Ba_{0.6}Sr_{0.4}Co_{0.7}Fe_{0.3}O_{3-\delta}$ ceramic membranes, Int. J. Hydrogen Energy 37 (2012) 12694–12699.
[43] K. Wiik, S. Aasland, H.L. Hansen, I.L. Tangen, R. Ødegard, Oxygen permeation in the system $SrFeO_{3-x}$–$SrCoO_{3-y}$, Solid State Ionics 152–153 (2002) 675–680.
[44] Y. Lu, H. Zhao, X. Cheng, Y. Jia, X. Du, M. Fang, Z. Du, K. Zheng, K. Swierczek, Investigation of In-doped $BaFeO_{3-\delta}$ perovskite-type oxygen permeable membranes, J. Mater. Chem. A 3 (2015) 6202–6214.
[45] G.Ch. Kostogloudis, N. Vasilakos, Ch. Ftikos, Crystal structure, thermal and electrical properties of $Pr_{1-x}Sr_xCoO_{3-\delta}$ ($x=0$, 0.15, 0.3, 0.4, 0.5) perovskite oxides, Solid State Ionics 106 (1998) 207–218.
[46] P. Meuffels, Propane gas sensing with high-density $SrTi_{0.6}Fe_{0.4}O_{(3-\delta)}$ ceramics evaluated by thermogravimetric analysis, J. Eur. Ceram. Soc. 27 (2007) 285–290.
[47] S. Lia, W. Jin, N. Xu, J. Shi, Mechanical strength, and oxygen and electronic transport properties of $SrCo_{0.4}Fe_{0.6}O_{3\text{-}d}$-YSZ membranes, J. Membr. Sci. 186 (2001) 195–204.
[48] B. Wei, Z. Lü, S. Li, Y. Liu, K. Liu, W. Su, Thermal and electrical properties of new cathode material $Ba_{0.5}Sr_{0.5}Co_{0.8}Fe_{0.2}O_{3-\delta}$ for solid oxide fuel cells, Electrochem. Solid State Lett. 8 (2005) A428–A431.
[49] S. Yoo, S. Choi, J. Kim, J. Shin, G. Kim, Investigation of layered perovskite type $NdBa_{1-x}Sr_xCo_2O_{5+\delta}$ ($x = 0$, 0.25, 0.5, 0.75, and 1.0) cathodes for intermediate-temperature solid oxide fuel cells, Electrochim. Acta 100 (2013) 44–50.
[50] S. Park, S. Choi, J. Shin, G. Kim, Tradeoff optimization of electrochemical performance and thermal expansion for Co-based cathode material for intermediate-temperature solid oxide fuel cells, Electrochim. Acta 125 (2014) 683–690.
[51] X. Zhang, H. Hao, X. Hu, Electronic transport properties of $YBaCo_{2-x}Cu_xO_{5+\delta}$($0 \leqslant x \leqslant 1$) at high temperature, Phys. Rev. B 403 (2008) 3406–3409.
[52] S. Yoo, J.Y. Shin, G. Kim, Thermodynamic and electrical characteristics of $NdBaCo_2O_{5+\delta}$ at various oxidation and reduction states, J. Mater. Chem. 21 (2011) 439–443.
[53] Y. Takeda, R. Kanno, M. Noda, Y. Tomida, O. Yamamoto, Cathodic polarization phenomena of perovskite oxide electrodes with stabilized zirconia, J. Electrochem. Soc. 134 (1987) 2656–2661.
[54] A. Jaiswal, E.D. Wachsman, Bismuth-ruthenate-based cathodes for IT-SOFCs, J. Electrochem. Soc. 152 (2005) A787-A90.
[55] H. Fukunaga, M. Koyama, N. Takahashi, C. Wen, K. Yamada, Reaction model of dense $Sm_{0.5}Sr_{0.5}CoO_3$ as SOFC cathode, Solid State Ionics 132 (2000) 279–285.
[56] F.C. Meng, T. Xia, J. Wang, Z. Shi, J.P. Lian, H. Zhao, J.M. Bassat, J.C. Grenier, Evaluation of layered perovskites $YBa_1L_xSr_xCo_2O_{5+\delta}$ as cathodes for intermediate temperature solid oxide fuel cells, Int. J. Hydrogen Energy 39 (2014) 4531–4543.
[57] J. Kim, W.Y. Seo, J. Shin, M. Liu, G. Kim, Composite cathodes composed of $NdBa_{0.5}Sr_{0.5}Co_2O_{5+\delta}$ and $Ce_{0.9}Gd_{0.1}O1.95$ for intermediate-temperature solid oxide fuel cells, J. Mater. Chem. A 1 (2013) 515–519.
[58] J.T.S. Irvine, D. Neagu, M.C. Verbraeken, C. Chatzichristodoulou, C. Graves, M.B. Mogensen, Evolution of the electrochemical interface in high-temperature fuel cells and electrolysers, Nat. Energy (2016) 15014.
[59] Y.P. Fu, R.H. Chen, M.Y. Hsieh, A. Subardi, W.K. Chang, Double perovskite $LaSrCo_{1.6}Cu_{0.4}O_{5+\delta}$ cathode for IT-SOFCs with pulsed laser technique deposited Bi-layer electrolyte, J. Electrochem. Soc. 162 (2015) F1029–F1035.
[60] A.V. Call, J.G. Railsback, H. Wang, S.A. Barnett, Degradation of nano-scale cathodes: a new paradigm for selecting low-temperature solid oxide cell materials, Phys. Chem. Chem. Phys. 18 (2016) 13216–13222.
[61] K. Chen, S.P. Jiang, Review—Materials degradation of solid oxide electrolysis cells, J. Electrochem. Soc. 163 (2016) F3070–F3083.
[62] W.C. Jung, H.L. Tuller, Investigation of surface Sr segregation in model thin film solid oxide fuel cell perovskite electrodes, Energy Environ. Sci. 5 (2012)

5370–5378.
[63] Y. Leng, S.H. Chan, Q. Liu, Development of LSCF–GDC composite cathodes for low-temperature solid oxide fuel cells with thin film GDC electrolyte, Int. J. Hydrogen Energy 33 (2008) 3808–3817.
[64] K. Yi, L. Sun, Q. Li, T. Xia, L. Huo, H. Zhao, J. Li, Z. Lu¨, J.M. Bassat, A. Rougier, S. Fourcade, J.C. Grenier, Effect of Nd-deficiency on electrochemical properties of $NdBaCo_2O_{6-\delta}$ cathode for intermediate-temperature solid oxide fuel cells, Int. J. Hydrogen Energy 41 (2016) 10228–10238.
[65] Y. Zheng, Y. Zhang, F. Yu, Z. Pan, H. Yang, L. Guo, Ca and Fe co-doped $SmBaCo_2O_{5+\delta}$ layered perovskite as an efficient cathode for intermediate-temperature solid oxide fuel cells, J. Alloys Compd. 696 (2017) 964–970.
[66] T.H. Lee, K.Y. Park, N.I. Kim, S.J. Song, K.H. Hong, D. Ahn, A.K. Azad, J. Hwang, S. Bhattacharjee, S.C. Lee, H.T. Lim, J.Y. Park, Robust $NdBa_{0.5}Sr_{0.5}Co_{1.5}Fe_{0.5}O_{5+\delta}$ cathode material and its degradation prevention operating logic for intermediate temperatures solid oxide fuel cells, J. Power Sources 331 (2016) 495–506.